

Statistical Imprints of SZ Effects in the Cosmic Microwave Background

ASANTHA COORAY⁽¹⁾(²)(*), DANIEL BAUMANN⁽³⁾, KRIS SIGURDSON⁽¹⁾

⁽¹⁾ *Theoretical Astrophysics, California Institute of Technology, Pasadena, CA 91125, USA*

⁽²⁾ *Department of Physics and Astronomy, 4129 Frederick Reines Hall, University of California, Irvine, CA 92697, USA*

⁽³⁾ *Department of Physics, Jadwin Hall, Princeton University, Princeton, NJ 08544, USA*

Summary. — We review several aspects of the Sunyaev-Zel'dovich (SZ) effect associated with the large scale baryon distribution and its characteristic signatures in the statistics of cosmic microwave background (CMB) anisotropies. We discuss (1) the contributions to the angular power spectrum from the thermal and kinetic SZ effects, (2) the effect of SZ non-Gaussianities on cosmological parameter estimation, and (3) the SZ-induced CMB polarization towards galaxy clusters. We also discuss the extent to which recent measurements of small angular scale CMB anisotropy can be accounted for by SZ clusters and the potential use of SZ polarization towards large samples of galaxy clusters as a probe of dark energy parameters.

2	1.	Introduction
4	2.	Thermal SZ Contribution to the CMB Power Spectrum
9	2'1.	Halo Mass Function
10	2'2.	Dark Matter Density Profile
11	2'3.	Concentration-Mass Distribution
11	2'4.	Gas Pressure Profile
12	3.	Comparison with Current CMB Data
13	3'1.	Covariance
16	4.	Kinetic SZ Contribution to the CMB Power Spectrum
18	5.	SZ Contributions to the Polarized CMB
18	5'1.	CMB-induced Polarization towards Clusters
19	5'2.	Primordial Quadrupole
21	5'3.	Kinematic Quadrupole
22	5'4.	CMB-induced Cluster Polarization and Dark Energy
24	5'5.	Power Spectra of SZ Polarization

(*) asante@caltech.edu

1. – Introduction

The Sunyaev-Zel’dovich effect (SZ; [1]) is the upscattering of cosmic microwave background (CMB) photons as they pass through the hot gas of a galaxy cluster. This upscattering introduces frequency-dependent secondary temperature anisotropies in the CMB that are proportional to the integral of the electron pressure $\Pi_e = n_e k_B T_e$ along a given line of sight through the Universe:

$$(1) \quad \frac{\Delta T^{\text{SZ}}}{T_{\text{CMB}}} \equiv g_\nu(x)y = g_\nu(x) \int d\eta a(\eta) \frac{\sigma_{\text{T}}}{m_e} \Pi_e(\eta).$$

where we have defined y , the Compton y -parameter, σ_{T} is the Thomson cross-section, and m_e is the electron rest-mass⁽¹⁾. The frequency dependence of the SZ anisotropies is accounted for by the function $g_\nu(x) = x \coth(\frac{x}{2}) - 4$ with $x = h\nu(k_B T_{\text{CMB}})^{-1}$, which, in the low frequency Rayleigh-Jeans part of the spectrum has the limit $g_\nu \rightarrow -2$. This form for the frequency spectrum leads to an apparent temperature decrement, relative to the primordial CMB black body spectrum, at frequencies below the null at x_{cross} , and an increment above x_{cross} . This SZ null occurs at approximately 217 GHz with a slight dependence on the electron temperature T_e due to higher-order relativistic corrections to the inverse-Compton scattering process neglected in the Thomson approximation. In Eq. (1), $\eta \equiv \eta(z)$ is the conformal distance from the observer at redshift $z = 0$ to the cluster at redshift z , given by

$$(2) \quad \eta(z) = \int_0^z \frac{dz'}{H(z')},$$

where the expansion rate of cold dark matter (CDM) cosmological models with a cosmological constant Λ is

$$(3) \quad H^2 = H_0^2 [\Omega_m(1+z)^3 + \Omega_K(1+z)^2 + \Omega_\Lambda].$$

The Hubble distance today is $H_0^{-1} = 2997.9 h^{-1} \text{Mpc}$ with $h = 0.72 \pm 0.08$ [2, 3]. Ω_i denotes the contribution of component i in units of the critical density $\rho_{\text{crit}} \equiv 3H_0^2/8\pi G$, with $i = c$ for the CDM, b for the baryons, and Λ for the cosmological constant. We also define the auxiliary quantities $\Omega_m \equiv \Omega_c + \Omega_b$ and $\Omega_K \equiv 1 - \sum_i \Omega_i$, which represent the total matter density and the contribution of spatial curvature to the expansion rate, respectively.

The thermal SZ effect has been imaged in the CMB towards massive galaxy clusters whose presence is a priori known from optical data [4, 5]. The temperature of the scattering medium in certain clusters can reach up to 10 keV producing temperature changes in the CMB of order 1 mK at Rayleigh-Jeans (RJ) wavelengths. The individual galaxy cluster SZ images have a variety of astrophysical and cosmological applications including a direct measurement of the angular diameter distance to the cluster through a combined analysis with X-ray data and a measurement of the gas mass, and, thus the baryon fraction of the universe. We do not discuss these applications of the SZ effect in the present review, but rather will concentrate on the statistical study of wide-field

⁽¹⁾ Note that here and in what follows we adopt units where the speed of light c is set to unity.

CMB data where SZ effects lead to anisotropies in the temperature distribution both due to resolved and unresolved galaxy clusters. In fact, the thermal SZ contribution is the dominant signal beyond the damping tail of the primary anisotropy power spectrum.

In addition to the thermal SZ effect, the bulk flow of electrons in galaxy clusters and other virialized halos that scatter the CMB photons leads to a second contribution to temperature fluctuations, the kinetic SZ effect. This effect arises from the well known Doppler effect [6, 7]:

$$(4) \quad \frac{\Delta T^{\text{dop}}}{T_{\text{CMB}}}(\hat{\mathbf{n}}) = \int_0^{\eta_0} d\eta g(\eta) \hat{\mathbf{n}} \cdot \mathbf{v}_g(\eta, \hat{\mathbf{n}}\eta),$$

where \mathbf{v}_g is the baryon velocity and $g(\eta)$ is the visibility function (also interpreted as the probability of scattering within $d\eta$ of η)

$$(5) \quad g = \dot{\tau} e^{-\tau} = X_e(z) H_0 \tau_H (1+z)^2 e^{-\tau}.$$

Here $\tau(\eta) = \int_0^\eta d\eta' \dot{\tau}(\eta')$ is the optical depth out to distance η , $X_e(z)$ is the ionization fraction as a function of redshift, and

$$(6) \quad \tau_H = 0.0691(1 - Y_p)\Omega_b h,$$

is the optical depth due to Thomson scattering to the Hubble distance today, assuming full hydrogen ionization with primordial helium fraction of $Y_p (= 0.24)$. From equation (4) follows the secondary temperature anisotropy due to the kinetic SZ effect. The kinetic SZ fluctuation is written as an integral over the product of the radial velocity, $\hat{\mathbf{n}} \cdot \mathbf{v}_g$, and the density fluctuation associated with the cluster, δ_g :

$$(7) \quad \frac{\Delta T^{\text{KinSZ}}}{T_{\text{CMB}}}(\hat{\mathbf{n}}) = \int_0^{\eta_0} d\eta g(\eta) \hat{\mathbf{n}} \cdot \mathbf{v}_g(\eta, \hat{\mathbf{n}}\eta) \cdot \delta_g(\eta, \hat{\mathbf{n}}\eta).$$

The angular power spectrum of anisotropies generated by the Doppler effect peaks at angular scales corresponding to the horizon at the time of scattering. The effect cancels out significantly at scales smaller than the horizon since photons scatter against the crests and troughs of the perturbation. The kinetic SZ effect arises from the second-order modulation of the Doppler effect by non-linear density fluctuations associated with virialized objects such as galaxy clusters, and avoids the strong cancellation associated with the linear Doppler effect. The kinetic SZ effect is also known as the Ostriker-Vishniac effect [8] when the density fluctuations are associated with the linear density field of the large-scale structure. In addition to modulation of the velocity field due to density perturbations, the velocity field is also modulated by fluctuations in the ionization fraction of electrons in a partly reionized universe during the reionization epoch. This latter contribution is generally referred to as patchy-reionization [9, 10, 11]. Due to the density weighting, the kinetic SZ effect peaks at small angular scales (sub arcminutes for Λ CDM). For a fully ionized universe, contributions are broadly distributed in redshift so that the power spectra are moderately dependent on the optical depth τ .

In this review we focus on the statistical characterization of secondary CMB temperature fluctuations in the form of the angular power spectrum of SZ-induced anisotropies.

Fig. 1. – The complex distribution of dark matter (a) found in numerical simulations may be replaced with a distribution of dark matter halos (b) with the mass function matching that found in simulations.

SZ maps have important additional applications including number counts of halos where a comparison to analytical predictions can be used to derive cosmological parameters. These studies will not be the subject of this short review, but are discussed elsewhere in these proceedings.

The outline of this article is as follows. In §2 we derive the power spectrum of the thermal SZ effect using the halo model of large scale structure. §3 compares these theoretical predictions to the current CMB data. In §4 we derive the power spectrum of the kinetic SZ effect. Finally, we discuss secondary CMB polarization due to free electrons in galaxy clusters and its cosmological use as a powerful probe of dark energy in §5.

2. – Thermal SZ Contribution to the CMB Power Spectrum

This section reviews the thermal SZ contribution to the angular power spectrum of CMB anisotropies following standard derivations published in the literature [12, 13, 14, 15].

The basic idea of the halo approach to large scale structure is summarized in Fig. 1. The complex dark matter distribution is replaced by a population of dark matter halos that reproduces the relevant statistical properties of the actual distribution [16]. The SZ anisotropy calculation is particularly well suited for the halo approach since high resolution simulations of the hydrodynamics of clusters, including radiative cooling and feedback from supernovae and galactic winds, indicate that nearly all of the power at small scales originates from regions associated with virialized halos rather than from filamentary structures or the diffuse gas between halos [18]. The semi-analytic calculations of Refs. [15, 17] are extended here by accounting for the self-gravity of the cluster gas and allowing for scatter in the concentration-mass distribution.

To calculate the angular power spectrum associated with the thermal SZ effect, it is

convenient to describe statistics in terms of the baryon gas pressure Π_g , which is related to the pressure of the electrons in the cluster by $\Pi_e(r) = \frac{2X+2}{3X+5}\Pi_g(r)$, where $X = 0.76$ is the primordial hydrogen abundance. We consider the difference in the local gas pressure relative to the mean pressure averaged over all positions, at a given epoch, and write the fluctuation as $\delta_\Pi(\mathbf{x}, t) \equiv (\Pi - \bar{\Pi})/\bar{\Pi}$, where Π denotes Π_e or Π_g . The mean value of δ_Π vanishes by definition:

$$(8) \quad \langle \delta_\Pi \rangle = \lim_{R \rightarrow \infty} \frac{\int_{|\mathbf{x}| < R} d^3\mathbf{x} \delta_\Pi(\mathbf{x})}{4/3\pi R^3} = 0.$$

The correlation function of pressure fluctuations is defined as $\xi(x) \equiv \langle \delta_\Pi(\mathbf{x}_1)\delta_\Pi(\mathbf{x}_2) \rangle$, where homogeneity and isotropy imply that correlations only depend on the absolute separation of the two locations, $x \equiv |\mathbf{x}_1 - \mathbf{x}_2|$. If the fluctuations are Gaussian, i.e. the random field related to δ_Π has a Gaussian probability distribution, then the distribution function is fully specified by the correlation function alone. A generic prediction of inflationary cosmology is the Gaussianity of the spectrum of initial fluctuations. However, non-linear growth and the formation of virialized halos lead to significant non-Gaussianity in the pressure field at the low redshifts probed by the SZ effect. Hence, to fully specify the statistics of the SZ power spectrum one must make measurements beyond the correlation function.

Instead of the real space correlation function, we will discuss statistics primarily in Fourier space where the fluctuation in pressure is

$$(9) \quad \delta_\Pi(\mathbf{k}) = \int d^3\mathbf{x} \delta_\Pi(\mathbf{x}) e^{-i\mathbf{k}\cdot\mathbf{x}}.$$

It is easily shown that Gaussianity of $\delta_\Pi(\mathbf{x})$ implies Gaussianity of $\delta_\Pi(\mathbf{k})$. We define the three-dimensional power spectrum of pressure fluctuations in the large scale structure as

$$(10) \quad \langle \delta_\Pi(\mathbf{k})\delta_\Pi(\mathbf{k}') \rangle \equiv (2\pi)^3 \delta_D(\mathbf{k} - \mathbf{k}') P_{\Pi\Pi}(k).$$

The Dirac delta function δ_D expresses the fact that wave modes \mathbf{k} and \mathbf{k}' are independent and uncorrelated since the different $\delta_\Pi(\mathbf{k})$ have random phases. Spatial isotropy requires the power spectrum to be independent of the phase of the wave vector and depend only on the magnitude of the vector. The power spectrum and the correlation function are related via

$$(11) \quad P_{\Pi\Pi}(k) = \int d^3\mathbf{x} \xi(x) e^{-i\mathbf{k}\cdot\mathbf{x}} = \int dx 4\pi x^2 \xi(x) \frac{\sin(kx)}{kx}.$$

The halo model for large scale structure predicts two separate contributions to the power spectrum:

$$(12) \quad P_{\Pi\Pi}(k; z) = P_{\Pi\Pi}^{1h}(k; z) + P_{\Pi\Pi}^{2h}(k; z),$$

where

$$(13) \quad \begin{aligned} P_{\Pi\Pi}^{1h}(k; z) &= I_{2, \Pi\Pi}^0(k; z), \quad \text{and} \\ P_{\Pi\Pi}^{2h}(k; z) &= [I_{1, \Pi\Pi}^1(k; z)]^2 P(k; z), \end{aligned}$$

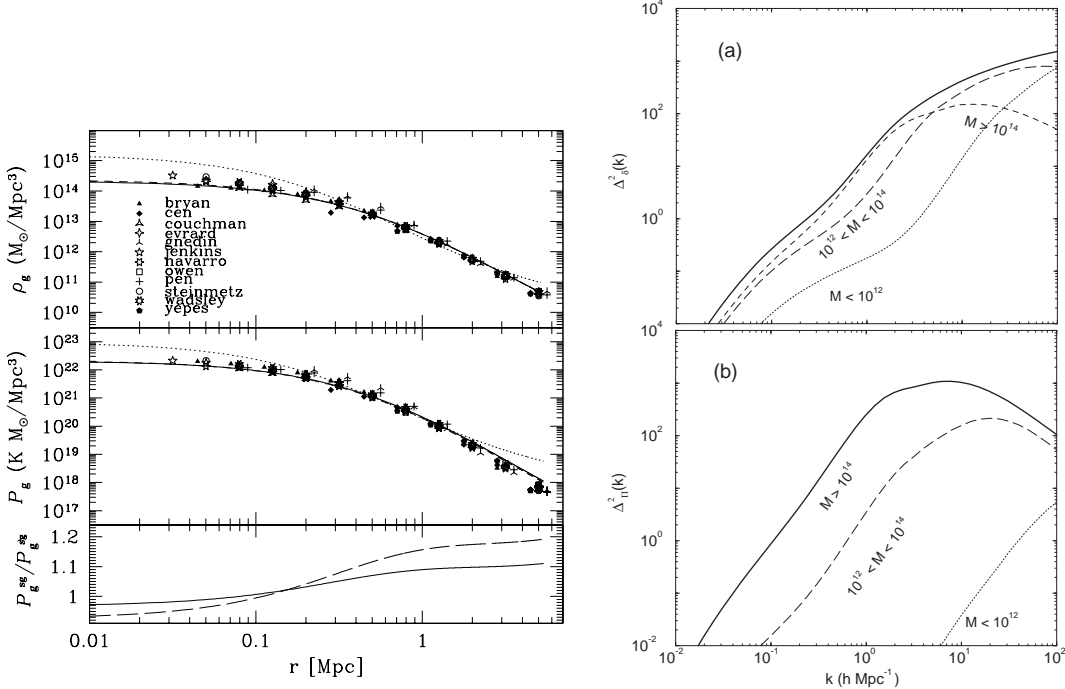


Fig. 2. – *Left*: The density (top) and pressure (middle) profiles for the self-consistent self-gravitational model (solid) and the isothermal cluster model (dotted) compared with numerical simulations from the Santa Barbara cluster comparison project. The isothermal model overestimates the pressure and density in the inner and outer regions of the cluster. The lower panel shows the ratio of the pressure profile calculated with self-gravity to the profile calculated without self-gravity for $f_b = 1/10$ (solid), the value used in the Santa Barbara cluster comparison project, and $f_b = 1/6$ (long-dashed), our fiducial value. Self-gravity raises the pressure by $\approx 20\%$ outside the core for our fiducial value. *Right*: The mass dependence on the dark matter power spectrum (a) and the pressure power spectrum (b). Here, we show the total contribution broken up into mass limits as labeled in the figure. As shown in (a), the large scale contribution to the dark matter power comes from massive halos while small mass halos contribute at small scales. For the pressure, in (b), only massive halos above a mass of $10^{14} M_\odot$ contribute to the power.

denote the power spectrum for correlations of gas pressure within a single halo (1h) and between two separate halos (2h). It is found that the 1-halo term dominates on small angular scales. The functions $I_{2,\text{III}}^0$ and $I_{1,\text{III}}^1$ are defined below and $P(k; z)$ is the linear matter power spectrum as a function of redshift z . Useful fitting formulae for the transfer function relating $P(k; z)$ to the primordial power spectrum $P(k)$ may be found in Ref. [19].

Using the three-dimensional Fourier transform of the (spherically symmetric) halo pressure profile $\Pi(r)$,

$$(14) \quad \Pi_e(k) = \int d^3\mathbf{r} \Pi_e(r) e^{-i\mathbf{k}\cdot\mathbf{x}} = \int_0^\infty dr 4\pi r^2 \Pi_e(r) \frac{\sin(kr)}{kr},$$

we can write the two I -terms in Eq. (13) as

$$(15) \quad \begin{aligned} I_{2,\text{III}}^0(k; z) &\equiv \int dM \int dc \frac{d^2 n}{dM dc} |\Pi_e(k, M, c; z)|^2 \quad \text{and} \\ I_{1,\text{III}}^1(k; z) &\equiv \int dM \int dc \frac{d^2 n}{dM dc} b_1(M; z) \Pi_e(k, M, c; z). \end{aligned}$$

Here, $d^2 n/dM dc$ is the bivariate halo mass function, the co-moving number density n of halos between mass M and $M + dM$ with concentration parameter between c and $c + dc$. The concentration parameter $c = r_v/r_s$ is defined as the ratio of the virial radius of the cluster r_v and a characteristic scale radius r_s . In writing Eq. (13), we assumed that halos trace the linear density field such that the halo power spectrum is $P_{\text{hh}}(k; z|M) = b_1^2(M)P(k; z)$ where M denotes the halo mass and the halo bias $b_1(M; z)$ is [20]

$$(16) \quad b_1(M; z) = 1 + \frac{a\nu^2(M; z) - 1}{\delta_c(z)} + \frac{2p}{\delta_c(z)\{1 + [a\nu^2(M; z)]^p\}},$$

where (a, p) are numerical parameters and $\nu(M; z) \equiv \delta_c(z)/\sigma(M; z)$ as discussed in more detail in section 2.1. We see from Eq. (15) that the two ingredients involved in calculating the power spectrum with the halo model are the radial pressure profile of the gas within each halo and the mass function, which specifies the number of such halos.

The angular power spectrum of the thermal SZ effect is just proportional to a projection of the three dimensional pressure power spectrum integrated along the line of sight. To derive the angular spectrum, we take spherical harmonics of Eq. (1) such that

$$(17) \quad \frac{\Delta T}{T}(\hat{\mathbf{n}}) = \sum_{lm} \left(\frac{\Delta T}{T} \right)_{lm} Y_{lm}(\hat{\mathbf{n}}).$$

Making use of the Rayleigh expansion of a plane wave

$$(18) \quad e^{i\mathbf{k}\cdot\hat{\mathbf{n}}\eta} = 4\pi \sum_{lm} i^l j_l(k\eta) Y_{lm}^*(\hat{\mathbf{k}}) Y_{lm}(\hat{\mathbf{n}}),$$

we find the spherical harmonic moments of the SZ map

$$(19) \quad \left(\frac{\Delta T}{T} \right)_{lm} = g_\nu \frac{\sigma_T}{m_e} 4\pi i^l \int \frac{d^3 \mathbf{k}}{(2\pi)^3} \Pi_e(\mathbf{k}) Y_{lm}^*(\hat{\mathbf{k}}) \int d\eta a^{-2}(\eta) j_l(k\eta).$$

The angular power spectrum of the SZ map, is defined in terms of multipole moments $[\Delta T/T]_{lm}$ as

$$(20) \quad \langle [\Delta T/T]_{lm} [\Delta T/T]_{l'm'}^* \rangle = C_l^{\text{SZ}} \delta_{ll'} \delta_{mm'}.$$

Using equation (19) and the relation $\langle \Pi_e(\mathbf{k}) \Pi_e(\mathbf{k}') \rangle = \bar{\Pi}_e^2 [\langle \delta_\Pi(\mathbf{k}) \delta_\Pi(\mathbf{k}') \rangle + 1]$ we obtain

$$C_l^{\text{SZ}} = g_\nu^2 \left(\frac{\sigma_T}{m_e} \right)^2 [\bar{n}_e(0)]^2 \frac{2}{\pi} \int k^2 dk P_{\text{III}}(k) \times$$

$$(21) \quad \times \int d\eta_1 \int d\eta_2 a^{-2}(\eta_1) a^{-2}(\eta_2) j_l(k\eta_1) j_l(k\eta_2),$$

where $\bar{n}_e(0)$ is the mean electron density today and we used $\bar{n}_e(\eta) = \bar{n}_e(0)a(\eta)^{-3}$.

With the Limber approximation [21], or, equivalently using an approximate identity related to the completeness of spherical Bessel functions

$$(22) \quad \int dk k^2 F(k) j_l(k\eta) j_l(k\eta') \approx \frac{\pi}{2} d_A^{-2} \delta_D(\eta - \eta') F(k)|_{k=l/d_A},$$

the projected SZ power spectrum can be written as

$$(23) \quad C_l^{\text{SZ}} = \int dr \frac{W^{\text{SZ}}(r)^2}{d_A^2(r)} P_{\text{III}} \left(k = \frac{l}{d_A(r)}; z(r) \right),$$

where d_A is the comoving angular-diameter distance, which in the case of a flat-cosmological model is $d_A = \eta$. We have defined the SZ weight function

$$(24) \quad W^{\text{SZ}}(\eta) \equiv g_\nu \frac{\sigma_T}{m_e} \frac{k_B \bar{n}_e(0)}{a(\eta)^2}.$$

The Limber approximation assumes that $F(k)$ is a slowly varying function when compared to oscillations in $j_l(x)$. Under this assumption, contributions to the power spectrum arise only from correlations on equal time slices of spacetime.

Given that the three-dimensional power spectrum of pressure can be written as a combination of 1- and 2-halo terms and the fact that the 1-halo term dominates the fluctuations, we can simplify the integral further and write it as [15]

$$(25) \quad C_l^{\text{SZ}} = \int dz \frac{d^2 V}{dz d\Omega} \int dM \int dc \frac{d^2 n}{dM dc} \Pi_l^2(z),$$

where $d^2 V/dz d\Omega$ is the physical volume per unit redshift per unit solid angle and Π_l is related to the three-dimensional Fourier transform of the electron pressure profile via

$$(26) \quad \Pi_l(z) = \frac{W^{\text{SZ}}(z) \Pi_e \left(k = \frac{l}{d_A}, z \right)}{d_A^2}.$$

Using the projected angular size of a cluster $\theta = r/d_A$, one can simplify further and reduce $\Pi_l(z)$ to the following two-dimensional integral

$$(27) \quad \Pi_l(z) = 2\pi W^{\text{SZ}}(z) \int_0^{\theta_{\text{out}}} \theta d\theta J_0 \left[\left(l + \frac{1}{2} \right) \theta \right] \int_{-r_{\text{out}}}^{+r_{\text{out}}} \Pi(r_{\parallel}, r_{\perp} = d_A \theta) dr_{\parallel},$$

where we have rewritten the volume integral Eq. 14 in terms of two separate integrals involving the line of sight distance through an individual halo, r_{\parallel} , and the 2-dimensional projected extent of the cluster, $r_{\perp} = d_A \theta$. Here, r_{out} is the outer radius of the halo,

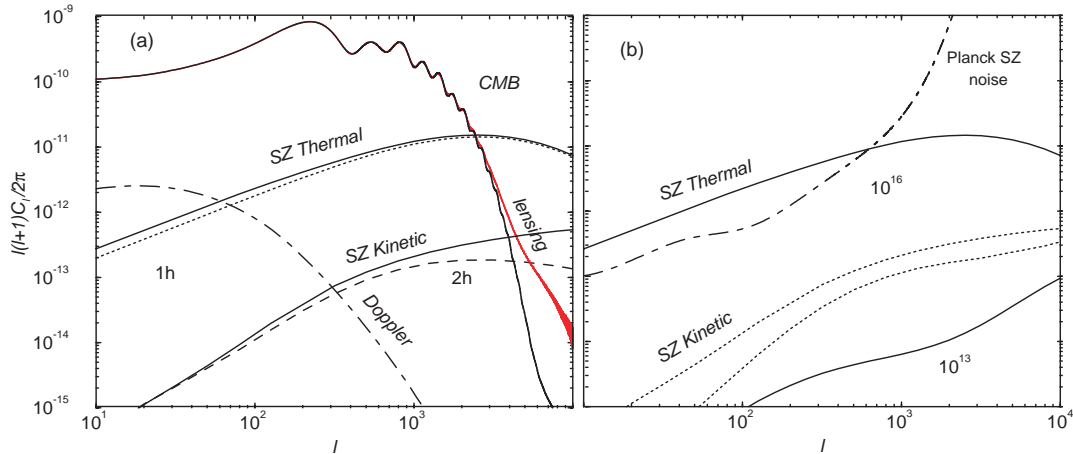


Fig. 3. – The angular power spectra associated with the thermal and kinetic SZ effects. As shown in (a), the thermal SZ effect is dominated by individual halos, and thus, by the single halo term (1h, dotted line), while the kinetic effect is dominated by the large scale structure correlations depicted by the 2-halo term (2h, dashed line). In (b), we show the mass dependence of the thermal and kinetic SZ effects with a maximum mass of 10^{16} and $10^{13} M_{\odot}$. The thermal SZ effect (solid lines) is strongly dependent on the maximum mass, while the kinetic effect (dotted lines) is not since it receives most of its contribution from large scale correlations.

which with a pressure profile that falls off with distance can be taken as $r_{\text{out}} \rightarrow \infty$, while $\theta_{\text{out}} = r_{\text{out}}/d_A$.

We now describe the ingredients required for the halo-based calculation of the SZ power spectrum in detail.

2.1. Halo Mass Function. – The mass function of the halo distribution is derived from the Press-Schechter formalism [22]. Press-Schechter theory is based on the idea that fluctuations in the linear density field with $\delta > \delta_c$ detach from the local Hubble expansion of the universe and collapse to form non-linear structure. The prediction for the fraction of the volume that has collapsed is

$$(28) \quad f_{\text{coll}}(M(R), z) = \frac{2}{\sqrt{2\pi}\sigma(R, z)} \int_{\delta_c}^{\infty} d\delta e^{-\delta^2/2\sigma^2(R, z)},$$

where R is the radius over which the density field has been smoothed, which is related to the halo mass by $M(R) = \rho_m \frac{4\pi}{3} R^3$ with ρ_m the co-moving matter density of the universe. The number density of halos is then found to be given by [22, 23]

$$(29) \quad \frac{dn(M, z)}{dM} = -\frac{\rho_m}{M} \frac{df_{\text{coll}}(M(R), z)}{dM} = \frac{\rho_m}{M} f(\nu) \frac{d\nu}{dM},$$

where

$$(30) \quad f(\nu) \equiv \sqrt{\frac{2A^2 a^2}{\pi}} [1 + (a\nu^2)^{-p}] e^{-\frac{a\nu^2}{2}}.$$

Here

$$(31) \quad \nu(M; z) \equiv \frac{\delta_c(z)}{\sigma(M; z)},$$

and

$$(32) \quad \delta_c(z) \simeq \frac{3(12\pi)^{\frac{2}{3}}}{20} \left[1 - \frac{5}{936} \ln \left(1 + \frac{1 - \Omega_m}{\Omega_m(1+z)^3} \right) \right]$$

is the critical density required for spherical collapse at a redshift z in a flat Λ CDM model (see e.g. Ref. [24] and references therein for this and related formulae). The variance in the density field smoothed with a top-hat filter of radius $R = (3M/4\pi\rho_m)^{\frac{1}{3}}$ is

$$(33) \quad \sigma^2(M; z) = G^2(z) \int \frac{dk}{k} \frac{k^3 P(k)}{2\pi^2} |W(kR)|^2,$$

where

$$(34) \quad W(x) = \frac{3}{x^3} [\sin(x) - x\cos(x)],$$

$P(k)$ is the linear matter power spectrum, and

$$(35) \quad G(z) = \frac{H(z) \int_z^\infty dz' (1+z') [H(z')]^{-3}}{H_0 \int_0^\infty dz' (1+z') [H(z')]^{-3}}$$

is the linear theory growth factor (often also denoted $D(z)$). A , p , and a in equation (30) are constants, with the canonical Press-Schechter (PS) and Sheth-Tormen (ST) mass functions corresponding to the parameters ($p = 0, a = 1$) and ($p = 0.3, a = 0.707$), respectively. The normalization A is determined by requiring mass conservation such that

$$(36) \quad \frac{1}{\rho_m} \int_0^\infty dM M \frac{dn}{dM} = \int_0^\infty d\nu f(\nu) = 1.$$

2.2. Dark Matter Density Profile. – The halo mass function has to be supplemented by the dark matter density profile. We define the dimensionless variable $u \equiv r/r_s$, where r_s is a characteristic scale radius. The dark matter profile within each halo is then defined as an NFW profile [25]

$$(37) \quad \rho_d(r) \equiv \rho_s \varrho_d(u) = \rho_s u^{-1} (1+u)^{-2}.$$

Within the context of the spherical collapse model, the outer extent of the cluster is taken to be the virial radius

$$(38) \quad r_v = \left[\frac{3M}{4\pi\rho_m(z)\Delta(z)} \right]^{\frac{1}{3}},$$

where $\rho_m(z) \propto (1+z)^3$ is the mean background matter density of the universe at redshift z , and

$$(39) \quad \Delta(z) \simeq 18\pi^2 \left[1 + \frac{88}{215} \left(\frac{1 - \Omega_m}{\Omega_m(1+z)^3} \right)^{\frac{86}{95}} \right]$$

is the overdensity of the halo relative to the background density [24]. The ratio of the virial radius to the scale radius is called the concentration parameter $c \equiv r_v/r_s$. Together, c and M completely determine the dark matter distribution of a given halo.

2.3. Concentration-Mass Distribution. – Numerical simulations indicate that clusters of a given halo mass have a range of concentration parameters. To account for this distribution we describe the number density of halos of mass M and concentration c by the bivariate distribution function,

$$(40) \quad \frac{d^2n}{dMdc}(M, c; z) \equiv \frac{dn}{dM}(M; z) \mathcal{P}(c|M; z),$$

where $\mathcal{P}(c|M; z)$ is the probability of a halo having concentration c given that it has mass M . Numerical simulations [26] find an approximately log-normal distribution

$$(41) \quad \mathcal{P}(c|M; z) dc = \frac{\exp\left(-\frac{[\log c - \log \bar{c}(M; z)]^2}{2\sigma_{\log c}^2}\right)}{\sqrt{2\pi}\sigma_{\log c}} \frac{dc}{\ln(10)c},$$

where the mean concentration parameter \bar{c} is related to the halo mass via

$$(42) \quad \bar{c}(M; z) = \frac{c_0}{1+z} \left[\frac{M}{M_*(z=0)} \right]^{-\alpha_c}.$$

$M_*(z)$ is the mass scale at which $\nu(M_*; z) = 1$ and c_0 and α_c are constants whose numerical values are typically chosen to be $c_0 = 9$ and $\alpha_c = 0.13$. It is in general possible that $\sigma_{\log c} = \sigma_{\log c}(M; z)$, as suggested by the scaling arguments of Ref. [27] and indeed a mass dependence has been noted in numerical simulations [26]. However, for simplicity we fix the width of the concentration distribution to be $\sigma_{\log c} = 0.14$ independent of mass.

2.4. Gas Pressure Profile. – The gas density profile in terms of the dimensionless parameter u is $\rho_g(r) \equiv \rho_0 \varrho_g(u)$. The isothermal assumption for the gas distribution used in Refs. [13, 14] was found to be inconsistent with the properties of numerically simulated clusters [17]. We therefore implement a polytropic equation of state and write the gas pressure as

$$(43) \quad P_g(r) \equiv P_0 p(u) = P_0 [\varrho_g(u)]^\gamma,$$

with $\varrho_g(0) = p(0) = 1$, so that ρ_0 and P_0 correspond to the central density and pressure. The gas profile within each halo has to self-consistently satisfy hydrostatic equilibrium,

$$(44) \quad \frac{1}{\rho_g} \frac{dP_g}{dr} = -\frac{GM(r)}{r^2},$$

where $M(r) = \int_0^r dr' 4\pi r'^2 [\rho_g(r') + \rho_d(r')]$ is the total mass of baryonic gas and dark matter. Rewriting Eq. (44) in terms of the dimensionless variables we introduced above leads to the following second order differential equation

$$(45) \quad \frac{d}{du} \left[\gamma u^2 \varrho_g^{\gamma-2} \frac{d\varrho_g}{du} \right] = -\lambda u^2 [\varrho_d(u) + \beta \varrho_g(u)],$$

where

$$(46) \quad \beta \equiv \frac{\rho_0}{\rho_s}$$

and

$$(47) \quad \lambda \equiv \frac{4\pi G \rho_0 \rho_s r_s^2}{P_0}.$$

In general $\varrho_g = \varrho_g(u; \lambda, \beta, \gamma, c, f_b)$. To fix $\varrho_g(u; c, f_b)$ for a given halo of concentration c and cosmological baryon fraction $f_b = \Omega_b/\Omega_m$ we impose the boundary condition that the gas density profile traces the dark matter density profile in the outer region of the halo. This ansatz from Ref. [17] ensures that the hydrodynamical properties of the cluster resemble those found in simulations of clusters which include both gas and dark matter. In order to implement this boundary condition and determine $\lambda(c; f_b)$, $\beta(c; f_b)$, and $\gamma(c; f_b)$, we minimize the functional

$$(48) \quad \Psi[\varrho_g(u; \lambda, \beta, \gamma, c, f_b)] = \int_{\frac{1}{2}c}^{2c} \frac{du}{u} [s_g(u) - s_d(u)]^2,$$

subject to the normalization constraint

$$(49) \quad \frac{\rho_g(r_v)}{\rho_d(r_v)} = \frac{\Omega_b}{\Omega_d} = \beta c(1+c)^2 \varrho_g(c),$$

where $s(u) = d \ln \varrho / d \ln u$ is the local logarithmic slope of the density profile $\varrho(u)$. We find that this procedure matches that of Ref. [17] when the gas self-gravity is neglected.

In Fig. 2 (left panel), we present a brief comparison of our model and the isothermal model with results from numerical simulations done as part of the Santa Barbara cluster comparison project [28]. As shown in Fig. 2, the isothermal cluster overestimates the gas density and pressure in the inner region and also shows a departure at the outer extent of the cluster. Comparing our model with that of Ref. [15] we see that including self-gravitational effects raises the pressure by $\sim 20\%$ outside the cluster core, which can increase the amplitude of the angular power spectrum of the SZ effect by as much as 25-30%.

3. – Comparison with Current CMB Data

In 2002, two significant results on CMB temperature fluctuations at arcminute angular scales appeared. The Cosmic Background Imager (CBI; [29]) and the Berkeley-Illinois-Maryland Array (BIMA; [30]) measured an excess of small-scale power beyond the damping tail of the primary CMB. Interpreting the CBI and BIMA results as low

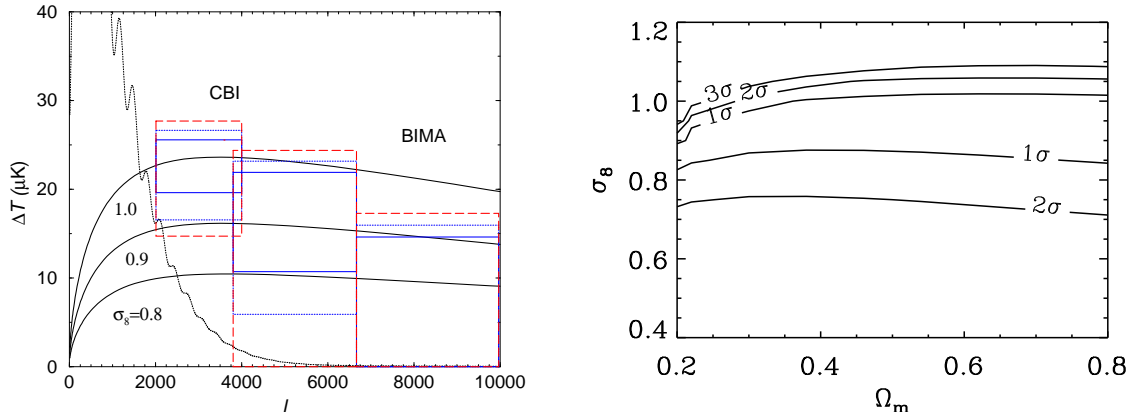


Fig. 4. – (a) Small-scale CMB anisotropies as observed by the CBI and BIMA experiments. The three solid lines show predictions for the SZ effect for varying σ_8 : 1.0 (upper), 0.9 (middle), and 0.8 (lower). For reference we show the predicted CMB primary anisotropies for our fiducial model. The solid error boxes show the published Gaussian errors, while the dotted boxes include the non-Gaussian trispectrum. When comparing data to predictions, we account for the full window function of these observations. (b) Constraints on cosmological parameters. We consider constraints on Ω_m and σ_8 using small-scale power and show 68%, 95%, and 99% confidence limits.

redshift SZ contributions to the temperature anisotropies allows constraints to be placed on cosmological parameters. The cosmological implications of the small-scale excess in CBI were first studied in Ref. [31] using numerical simulations of the SZ effect associated with unresolved clusters. A more detailed analysis of the small-scale CBI data, based on semi-analytic calculations, was presented in Ref. [15], where a constraint was placed on the normalization of the matter power spectrum σ_8 .

To study the constraints on cosmological parameters from small-scale anisotropies, one generally performs a likelihood analysis. Here, one must take into account the window functions of band-power from CBI and BIMA. In order to compare data to theoretical predictions, we calculate the relative χ^2 between data and models

$$(50) \quad \chi^2 = \sum_{i \leq j} (\hat{\mathcal{C}}_i - \mathcal{C}_i) C_{ij}^{-1} (\hat{\mathcal{C}}_j - \mathcal{C}_j),$$

where $\hat{\mathcal{C}}_i$ is a band-power estimate from recent observations, \mathcal{C}_i is the model prediction, and C_{ij}^{-1} is the inverse covariance matrix. As we will now discuss, due to the highly non-linear nature of galaxy clustering, one must take non-Gaussian contributions to the covariance into account.

3.1. Covariance. – The measurements of the power spectrum reported by the CBI and BIMA experiments are binned estimates of power in multipole space with window functions $W(\mathbf{l}_i)$ at each band i , where \mathbf{l}_i is a vector in a plane of the sky sufficiently small

to be considered flat. One can write these band-power estimates as

$$(51) \quad \hat{C}_i = \int \frac{d^2 \mathbf{l}_i}{A_i} W(\mathbf{l}_i) W(-\mathbf{l}_i) \hat{\Theta}(\mathbf{l}_i) \hat{\Theta}(-\mathbf{l}_i),$$

where $A_i = \int d^2 \mathbf{l}_i W^2(\mathbf{l}_i)$ is the window-weighted area of the two-dimensional shell in Fourier space and $\hat{\Theta}(\mathbf{l}_i)$ is the Fourier transform of temperature fluctuations $\hat{\Theta}(\hat{\mathbf{n}}) \equiv \Delta T/T(\hat{\mathbf{n}})$ in the SZ map. Following Ref. [32], we can write the covariance matrix of these band-power measurements as

$$(52) \quad C_{ij} = \frac{(2\pi)^2}{A} \left[\frac{2C_i^2}{A_i} \delta_{ij} + \frac{T_{ij}^{\text{SZ}}}{(2\pi)^2} \right],$$

where

$$(53) \quad T_{ij}^{\text{SZ}} = \int \frac{d^2 \mathbf{l}_i}{A_i} \int \frac{d^2 \mathbf{l}_j}{A_j} W^2(\mathbf{l}_i) W^2(\mathbf{l}_j) T_{\text{SZ}}(\mathbf{l}_i, \mathbf{l}_j)$$

and A is the total area of the survey in steradians. The first term in equation (52) is the usual Gaussian sample variance and the second term is the extra non-Gaussian contribution that arises from the trispectrum associated with the SZ effect. The Gaussian noise also includes an additional noise variance due to instrumental noise. In the case of CBI and BIMA, the first term, including instrumental noise, is generally determined during the band-power measurements. Thus, we only consider the extra covariance from the non-Gaussian contribution. We again use the halo approach to model this term. At the small scales relevant for current data, the one-halo term dominates [14]. We thus consider the trispectrum due to single halos,

$$(54) \quad T_{\text{SZ}}(\mathbf{l}_i, \mathbf{l}_j) \equiv T_{\text{SZ}}(\mathbf{l}_i, -\mathbf{l}_i, \mathbf{l}_j, -\mathbf{l}_j) = \int dr \frac{W^{\text{SZ}}(r)^3}{d_A^6(r)} T_{\text{III}}^{\text{1h}} \left(\frac{\mathbf{l}_i}{d_A(r)}, \frac{\mathbf{l}_j}{d_A(r)}; z(r) \right).$$

Note that the projected trispectrum is generally a function of four \mathbf{l} vectors and may therefore be represented by a general quadrilateral in Fourier space. In the case of the power spectrum covariance we are only interested in terms involving $T_{\text{SZ}}(\mathbf{l}_i, -\mathbf{l}_i, \mathbf{l}_j, -\mathbf{l}_j)$, i.e. parallelograms which are defined by either the length $l_{ij} = |\mathbf{l}_i - \mathbf{l}_j|$ or the angle between \mathbf{l}_i and \mathbf{l}_j . This can be noted from the fact that the correlator between $\langle \hat{C}_i \hat{C}_j \rangle$ involves the temperature fluctuations as $\langle \hat{\Theta}(\mathbf{l}_i) \hat{\Theta}(-\mathbf{l}_i) \hat{\Theta}(\mathbf{l}_j) \hat{\Theta}(-\mathbf{l}_j) \rangle$ which is simply equal to the trispectrum with the above dependence.

Under the halo model the trispectrum involves four terms related to configurations with 1 to 4 halos. On small scales the 1-halo term dominates, similar to the case of the power spectrum, and we can write this contribution to the trispectrum responsible for power spectrum covariance as

$$(55) \quad T_{\text{III}}^{\text{1h}}(\mathbf{k}_1, \mathbf{k}_2; z) = \int dM \int dc \frac{d^2 n}{dM dc} |\Pi(|\mathbf{k}_1|, M, c; z)|^2 |\Pi(|\mathbf{k}_2|, M, c; z)|^2.$$

In addition to the extra variance (when $|\mathbf{l}_i| = |\mathbf{l}_j|$), this non-Gaussian term also contributes to the covariance and correlates band-power measurements between different

bins (when $|\mathbf{l}_i| \neq |\mathbf{l}_j|$). Note that in the case of the 1-halo term, the trispectrum is independent of the angle between \mathbf{l}_i and \mathbf{l}_j and only depends on the amplitude of these two vectors, though, this is not the case in general when other terms, such as 2-halo and higher, are involved.

In Fig. 4, we show the extra variance contribution to the band-power estimates due to non-Gaussianities. These non-Gaussian errors are such that they decrease with increasing sky area of the survey and should be understood as arising from the rareness of galaxy clusters that contribute to the SZ anisotropies. In Fig. 4, we show the angular power spectrum of the SZ effect along with the primordial anisotropies for our fiducial cosmological model. Here we plot flat-band power per logarithmic interval in μK such that

$$(56) \quad \Delta T = \sqrt{\left(\frac{l(l+1)}{2\pi} C_l\right)} T_{\text{CMB}},$$

where $T_{\text{CMB}} = 2.726 \times 10^6 \mu\text{K}$. We also show flat-band power estimates of the anisotropies at small angular scales from CBI [29] and BIMA [30]. The two error boxes represent the Gaussian error published by both experimental groups and the total which includes the non-Gaussian error. For comparison, we show three predictions for the SZ power spectrum for σ_8 ranging from 0.9 to 1.1. In general the SZ angular power spectrum C_l^{SZ} scales approximately as $(\sigma_8)^7$ [33].

To extract cosmology, we consider a parameter set comprised only of (Ω_m, σ_8) , fixing all other cosmological parameters to fiducial values given by the WMAP best-fit [3]. The 1- σ and 2- σ constraints on this two-parameter space are shown in Fig. 4. Our constraints are consistent with those obtained by Ref. [15] and suggested in Ref. [31]. Marginalizing over values of Ω_m in the range of 0.14 to 0.96, we find $\sigma_8(\Omega_b h/0.036)^{0.3} = 0.95_{-0.23}^{+0.10}$ at 95% confidence. The data allow σ_8 values of around 1.0 to 0.85 at the 1 σ level, consistent with complementary cosmological measurements. The inclusion of self-gravity and the distribution in concentration increases power beyond the models in Ref. [17]. Note that our results, while consistent with results from the analysis in Ref. [34], still allow a larger range of values for σ_8 than suggested there.

While small scale anisotropies can be interpreted as being due to the thermal SZ effect, this interpretation is not unique. Arcminute-scale anisotropies can easily be generated at the surface of last scattering if the primordial power spectrum had a feature. It is, however, important to keep in mind that scale-dependent features in the primordial power spectrum may be unnatural in specific models of inflation. Other effects producing small-scale anisotropies include primordial voids at last scattering. If the reionization optical depth is high, as suggested by the recent WMAP results [46], and the reionization process is associated with massive stars, then a substantial small-scale signal could also be generated by the thermal SZ effect associated with the first supernova bubbles [35]. Similarly, at low redshifts, the secondary signal could be due to foreground sources such as unresolved point sources.

As discussed in Ref. [36], to uniquely determine if the contribution is associated with the thermal SZ effect, one needs to establish the frequency spectrum with multi-frequency observations, or consider cross-correlation studies with tracers of large scale structure. If the contribution is generated at last scattering, then one does not expect a significant correlation with, say, the low redshift galaxy distribution, while a strong correlation is expected, if arcminute scale fluctuations are related to the thermal SZ effect. A similar

cross-correlation analysis would be required to separate the thermal SZ effect in galaxy clusters from the effect related to the first supernovae. The latter signal would not be resolved, while with high resolution SZ maps, the removal of resolved SZ clusters will lead to a substantial decrease in the amplitude of the SZ power spectrum, by which the presence of SZ supernovae can be explored.

In addition to the power spectrum, due to the highly non-linear nature of the thermal SZ effect, a significant non-Gaussianity is induced by SZ contributions to arcminute-scale CMB fluctuations [7, 13, 14] which can be measured from the bispectrum, the three-point correlation function in Fourier space, or more easily, using measurements of the skewness, among others. The SZ effect is also strongly correlated with angular deflections associated with gravitational lensing modifications of CMB anisotropies [7, 37, 38]. Future experiments such as Planck will be able to measure some of these higher-order effects.

4. – Kinetic SZ Contribution to the CMB Power Spectrum

We next provide a brief discussion of the kinetic SZ contribution to the CMB power spectrum. The kinetic SZ effect results from the modulation of the large-scale velocity field by non-linear density structures such as galaxy clusters. In Fourier space, the effect is described as a convolution of the density and the velocity fluctuations (cf. Eq. (7)). If we consider the flat-sky limit in which the Limber approximation [21] applies, then we can write the associated power spectrum as

$$(57) \quad C_l^{\text{KinSZ}} = \frac{1}{8\pi^2} \int d\eta \frac{(g\dot{G})^2}{d_A^2} I_v \left(k = \frac{l}{d_A} \right).$$

Recall that $g(\eta)$ and $G(\eta)$ are the visibility function (5) and the linear growth function (35), respectively. The mode-coupling integral is given by

$$(58) \quad I_v(k) = \int dk_1 \int_{-1}^{+1} d\mu \frac{(1-\mu^2)(1-2\mu y_1)}{y_2^2} P_{\delta\delta}(ky_1) P_{gg}(ky_2),$$

where $P_{\delta\delta}$ and P_{gg} denote the power spectra of perturbations in the dark matter and the cluster gas densities, respectively. In the above, $\mu = \hat{\mathbf{k}} \cdot \hat{\mathbf{k}}_1$, $y_1 = k_1/k$ and $y_2 = k_2/k = \sqrt{1 - 2\mu y_1 + y_1^2}$. The wave vectors \mathbf{k}_1 and $\mathbf{k}_2 = \mathbf{k} - \mathbf{k}_1$ capture the convolution between velocity and gas density perturbations. We refer the reader to [8, 14, 39, 40, 41] for the details of the derivation of equations (57) and (58). The velocity field power spectrum is related to the linear dark matter density field through the use of linear theory arguments involving the continuity equation where $\mathbf{v} = -i\dot{G}\delta\mathbf{k}/k^2$, which was used in deriving Eq. (58).

Since velocity fluctuations have a much larger coherence length than the non-linear gas density fluctuations traced by galaxy clusters, we consider the limit in which the velocity field is uncorrelated with the clusters. Physically, this can be thought of as the limit in which large-scale bulk flows are modulated by small-scale overdensities. In this small-scale limit, the dominant contributions to the integrals in equations (57) and (58) arise from modes with $k_2 = |\mathbf{k} - \mathbf{k}_1| \sim k$ such that $y_1 \ll 1$ and $y_2 \rightarrow 1$, and equation

Fig. 5. – Line of sight projected maps of the thermal (left) and kinetic (right) SZ effects (Figures reproduced from Ref. [42]). The maps are $1^\circ \times 1^\circ$ and cover the same field of view. Note that the thermal SZ map picks out massive halos, while contributions to the kinetic SZ effect come from a wide range of masses. Unlike the thermal SZ effect, which produces a negative decrement at Rayleigh-Jeans wavelengths, the kinetic SZ effect varies between negative and positive values depending on the direction of the velocity field. Here, structures in red are moving towards the observer while those in blue are moving away.

(57) reduces to

$$(59) \quad C_l^{\text{KinSZ}} = \frac{1}{3} \int d\eta \frac{(g\dot{G})^2}{d_A^2} P_{gg}(k) v_{\text{rms}}^2,$$

where v_{rms}^2 is the rms of the (large scale) uniform bulk velocity

$$(60) \quad v_{\text{rms}}^2 \equiv \int dk \frac{P_{\delta\delta}(k)}{2\pi^2}.$$

The factor of 1/3 in Eq. (59) arises from the fact that the rms in each component is 1/3 of the total velocity.

Just as in the halo model calculation of the thermal SZ effect, we split the power spectrum of perturbations in the cluster gas densities into 1-halo and 2-halo terms, $P_{gg} \equiv P_{gg}^{1h} + P_{gg}^{2h}$. For the thermal SZ effect we found that the 1-halo term was the dominant contribution and that correlations between halos could be neglected. For the kinetic SZ effect, however, we find that the 2-halo correlation term is most important and the 1-halo term can be neglected. This is illustrated in Fig. 3, where we show our prediction for the CMB power spectrum associated with the kinetic SZ effect and a comparison with the thermal SZ contribution. It is observed that the kinetic SZ contribution is roughly an order of magnitude smaller than the thermal SZ contribution. We also see that the thermal SZ effect is dominated by individual halos, while the kinetic SZ effect is dominated by large scale structure correlations depicted by the 2-halo term. We understand these results as follows: The temperature anisotropies associated with the thermal SZ effect are proportional to the temperature weighted electron density (or the electron pressure, cf. equation (1)) and are therefore dominated by the most massive clusters with a correspondingly high electron temperature. The kinetic SZ contribution

is independent of the cluster temperature and depends only on the electron density and the cluster velocity. Contributions to the kinetic SZ effect therefore come from baryons tracing all scales down to small mass halos and the CMB power spectrum associated with the kinetic SZ rescattering is dominated by the large scale correlations of the halos.

The different mass dependence of the two effects suggests that wide-field thermal and kinetic SZ maps will show characteristic differences in that massive halos, or clusters, will be clearly visible in a map tracing the thermal SZ effect, while the large scale structure will be more evident in a kinetic SZ map. As shown in the thermal and kinetic SZ maps in Fig. 5 from [42], numerical simulations are in fact consistent with this picture (see also [43]).

In addition to the contribution due to the line of sight motion of halos, there is an effect resulting from halo rotations as discussed by [44]. Recent studies have considered this non-uniform motion of cluster gas with numerical simulations (e.g. [45]). The signal is considerably smaller than the bulk flow kinetic SZ effect and therefore unlikely to be of interest to current and next-generation measurements of arcminute-scale CMB anisotropies.

5. – SZ Contributions to the Polarized CMB

Polarization of CMB anisotropies is generated when the CMB photons scatter off free electrons. The polarization therefore traces the ionization history of the universe. The universe was fully ionized at early times, before last scattering occurred at a redshift of about $z_{\text{rec}} \approx 1100$, after which the universe became neutral and radiation and matter decoupled. Last scattering generated the *primary* polarization of the microwave background radiation. Since the generation of polarization is a strictly causal process this signal is expected to peak at the horizon scale at recombination. Causality doesn't allow a polarization signal on larger scales. Such a signal, however, has recently been measured by the Wilkinson Microwave Anisotropy Probe (WMAP) [46]. This *large-scale secondary* polarization is interpreted as a signature of a late time reionization of the universe at a redshift of $z \sim 10 - 20$. Since reionization leads to free electrons in galaxy clusters we also expect *small-scale* secondary polarization [47, 48]. In Ref. [49], we revisited the problem of measuring a CMB-induced polarization signal towards *resolved* galaxy clusters. This was previously studied by Refs. [1, 51, 52, 53].

Linear polarization of the cosmic microwave background is generated through rescattering of the temperature quadrupole. In a cosmological model with dark energy the quadrupole evolves between the last scattering surface ($z = 1100$) and us ($z = 0$) due to the integrated Sachs-Wolfe (ISW) effect. The quadrupole-induced polarization signal therefore provides an opportunity to probe dark energy through the ISW effect. Kamionkowski and Loeb [54, 55] have considered the possibility of using multiple such measurements to reduce the cosmic variance uncertainty in the CMB temperature quadrupole. The connection between properties of dark energy, the quadrupole at the cluster redshift and polarization in the direction of galaxy clusters is summarized here.

5.1. CMB-induced Polarization towards Clusters. – CMB polarization towards clusters is generated when the incident radiation has a non-zero temperature quadrupole moment. The two dominant origins for this quadrupole moment are: (a) a projection of the *primordial* CMB quadrupole to the cluster location, and (b) a local *kinematic* quadrupole from cluster peculiar motion. Towards a sufficiently large sample of galaxy clusters, we can write the total rms degree of polarization as $P_{\text{Total}}^2 = P_{\text{Prim}}^2 + P_{\text{Kin}}^2$,

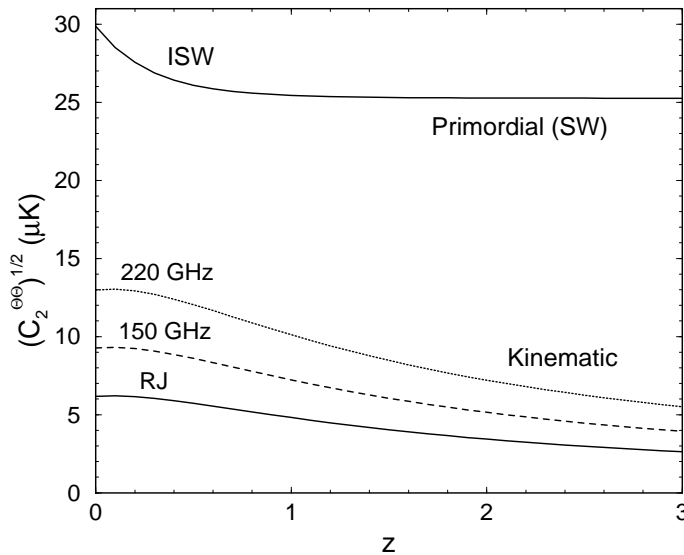


Fig. 6. – The temperature quadrupole, $C_2^{\Theta\Theta}$, ($\Theta \equiv \Delta T/T$), as a function of redshift. We show both the primordial and the kinematic quadrupole. The bottom kinematic-quadrupole curve is for $g(x) = 1$, as appropriate for the Rayleigh-Jeans (RJ) part of the frequency spectrum, and the dashed and dotted curves are, respectively, for frequencies 150 and 220 GHz.

Ref. [51], where

$$(61) \quad P_{\text{Prim}} \propto \langle \tau \rangle Q^{\text{rms}}(z) \propto \sqrt{C_2(z)},$$

$$(62) \quad P_{\text{Kin}} \propto g(x) \langle \tau \rangle \langle \beta_t^2 \rangle.$$

$\tau = \sigma_T \int d\ell n_e(\ell)$ is the scattering optical depth of a cluster with ℓ the physical line of sight distance through the cluster and $n_e(\ell)$ the electron number density. Since we are averaging over large samples of clusters, we consider the sample-averaged optical depth, $\langle \tau \rangle$. $\beta_t = v_t/c$ gives the transverse component of the cluster velocity and $g(x) = (x/2) \coth(x/2)$, with $x \equiv h\nu/k_B T_{\text{CMB}}$, is the frequency dependence of the kinematic effect. With the optical depth in individual clusters determined by complementary methods, such as the Sunyaev-Zel'dovich (SZ, [1]) effects, one can invert the measured polarization, equation (61), to obtain the rms CMB-quadrupole, $Q^{\text{rms}}(z) \equiv (5C_2/4\pi)^{1/2}$, at the cluster redshift.

5.2. Primordial Quadrupole. – The primordial CMB-quadrupole is dominated by two effects. The Sachs-Wolfe (SW, [56]) effect arises as a combination of gravitational redshift and time-dilation effects and can be viewed as a direct projection of the conditions at last scattering with no evolution after that time:

$$(63) \quad \left(\frac{\Delta T}{T} \right)^{\text{SW}} = \frac{\Phi(\eta = \eta_{\text{ls}})}{3},$$

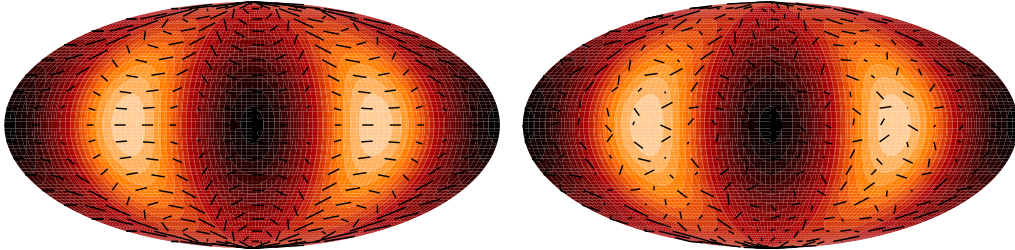


Fig. 7. – CMB polarization due to galaxy clusters. The polarization vectors give a representation of the expected polarization from a cluster at the corresponding location in the sky. The scale is such that the maximum length of a line corresponds to a polarization of $4.9\tau \mu\text{K}$, where τ is the optical depth of the cluster. The background color represents the temperature quadrupole. The left map shows the resulting polarization contribution due to scattering of the primordial temperature quadrupole alone. The map for the total polarization contribution (primordial and kinematic) is indistinguishable from this map. To make the kinematic polarization visible, we arbitrarily increase its amplitude by a factor of 100 (right map). The primordial polarization dominates the total contribution even at high frequencies where the kinematic quadrupole is boosted due to its spectral dependence.

where Φ is the Newtonian potential. The integrated Sachs-Wolfe (ISW) contribution arises along the photon path from the time of last scattering to today, as the CMB photons pass through a time-varying potential:

$$(64) \quad \left(\frac{\Delta T}{T}\right)^{\text{ISW}} = 2 \int_{\eta_{\text{ls}}}^{\eta_0} \dot{\Phi} d\eta.$$

Effectively, the photon receives a shift in energy because the potential it falls into is different from the potential it must climb out of. The ISW effect is absent in a matter-dominated, critical-density universe (Einstein-de Sitter). In a universe with dark energy ($w \equiv p/\rho < 0$) or a cosmological constant, Λ , ($w = -1$) the ISW effect leads to an increase in power on large scales. The expected redshift evolution of the quadrupole, $C_{l=2}(z) = C_{l=2}^{\text{SW}}(z) + C_{l=2}^{\text{ISW}}(z)$, is hence characterized by a rise at low redshifts ($z < 1$), the time at which the universe becomes dark energy dominated.

We calculate $C_2^{\Theta\Theta}(z)$, $\Theta \equiv \Delta T/T$, following Ref. [47] for our fiducial ΛCDM cosmology and show the result in Fig. 6. Note that at redshift $z = 0$, with the power-spectrum tilt fixed at unity, COBE finds $C_2^{\Theta\Theta}(z = 0) = (27.5 \pm 2.4 \mu\text{K})^2$ [57]. At higher redshifts, the mean quadrupole moment evolves due to the integrated Sachs-Wolfe effect and possibly, if the power spectrum is not flat, due to any scale dependence since the quadrupole probes smaller distances at earlier times. The primordial quadrupole has a coherence length comparable to the horizon. We thus expect the polarization signal measured on a $\mathcal{O}(10^\circ)$ patch of sky may differ by order unity from that on a different $\mathcal{O}(10^\circ)$ patch of sky. Finally, note that Thomson scattering from cold electrons will not change the photon frequency. Thus, there will be no frequency dependence of the rescattering of the primordial quadrupole.

5.3. Kinematic Quadrupole. – The origin of the kinematic polarization effect is understood as follows. Consider electrons moving with peculiar velocity, $\beta = v/c$, relative to the rest frame defined by the CMB. The Doppler-shifted spectral intensity of the CMB in the mean electron rest frame is

$$(65) \quad I_\nu = C \frac{x^3}{e^{x\gamma(1+\beta\mu)} - 1},$$

where $x \equiv h\nu/k_B T_{\text{CMB}}$, $\gamma = (1 - \beta^2)^{-1/2}$ and μ is the cosine of the angle between the cluster velocity and the direction of the incident CMB photon. When expanded in terms of Legendre polynomials, the intensity distribution is

$$(66) \quad I_\nu = C \frac{x^3}{e^x - 1} \left[I_0 + I_1 \mu + \frac{e^x(e^x + 1)}{2(e^x - 1)^2} x^2 \beta^2 \left(\mu^2 - \frac{1}{3} \right) + \dots \right],$$

which contains the necessary quadrupole component under which scattering generates polarization.

Unlike the primordial quadrupole, the kinematic quadrupole has a frequency dependence which we denote by $g(x)$, and using the expansion of the intensity distribution, in temperature units instead of intensity units, one can show $g(x) = (x/2) \coth(x/2)$.

The a_{22} quadrupole moment related to the cluster transverse motion (in a coordinate system in which z is along the line of sight) is

$$(67) \quad a_{22} = g(x) \sqrt{\frac{4\pi}{30}} v_t^2 e^{2i\phi_v},$$

where ϕ_v is the orientation angle for v_t on the plane of the sky. To obtain this result, note that in a coordinate system in which the $\hat{\mathbf{z}}$ axis is aligned with the cluster's motion, the quadrupole dependence of the radiation temperature is $g(x)v_t^2(\mu^2 - 1/3) = g(x)v_t^2(2/3)\sqrt{4\pi/5}Y_{2,0}$, where μ is the cosine of the angle between the radiation direction and the $\hat{\mathbf{z}}$ direction. However, in a coordinate system in which the $\hat{\mathbf{z}}$ axis is taken to be along the line of sight, $(\mu^2 - 1/3) = -(1/3)\sqrt{4\pi/5}Y_{2,0} + \sqrt{2\pi/15}(Y_{2,2} + Y_{2,-2})$. Thus, the coefficient of $Y_{2,2}$, the component of the quadrupole moment that gives rise to polarization in our direction, is only a fraction $\sqrt{3/8}$ of the total quadrupole moment.

Fig. 7 illustrates the primordial and kinematic quadrupole contributions using all-sky maps of the expected polarization. In these plots, each polarization vector should be considered as a representation of the polarization towards a cluster at that location. The polarization pattern created by scattering of the primordial quadrupole is uniform and traces the underlying temperature quadrupole distribution. For the kinematic quadrupole we assume, for illustrative purposes, a transverse velocity field with $\langle \beta_t \rangle \sim 10^{-3}$ corresponding to a velocity of 300 km sec $^{-1}$. The polarization contribution due to the kinematic quadrupole, however, is random due to the fact that transverse velocities are uncorrelated⁽²⁾. This explains the randomization of the all-sky polarization map when a significant kinematic contribution is included. It should be noted, however, that the kinematic effect has been scaled by a factor of 100 to make it visible in Fig. 7.

⁽²⁾ The correlation length of the velocity field (~ 60 Mpc) correlates velocities within regions of 1° when projected to a redshift of order unity.

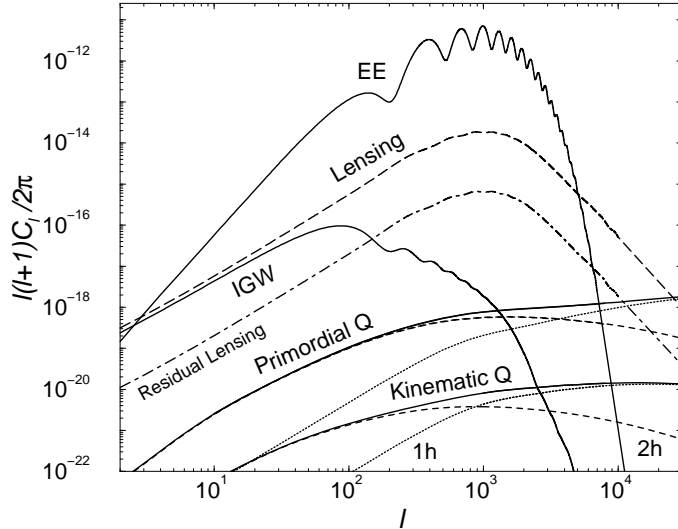


Fig. 8. – Polarization power spectra due to the rescattering of the primordial and kinematic quadrupoles. We break total power in each of these cases into the 1- (1h; dotted lines) and 2-halo (2h; dashed lines) terms under the halo-based approach used here. While at large angular scales correlations between halos dominate, at small angular scales of order few arcminutes and below, contributions are dominated by the 1-halo term. For comparison, we also show primordial polarization power spectra for E and B-modes involving dominant scalar (E-mode) and tensor (B-mode) contributions respectively. The tensor contribution to B-modes due to inflationary gravitational waves (IGW) assumes an energy scale for inflation of 10^{16} GeV. The long-dashed curve is the contribution to B-modes of polarization resulting from the cosmic shear conversion of power in E-modes, while the dot-dashed line labeled “Residual Lensing” represents the noise contribution after optimally subtracting the lensing contribution using higher-order statistics.

Therefore, as shown in Fig. 7, the primordial polarization dominates the total contribution even at high frequencies where the kinematic quadrupole is increased due to its spectral dependence. Also, the spectral dependence of the kinematic quadrupole contribution, $g(x)$, gives a potential method to separate the two polarization effects [58]. This is similar to component separation suggestions in the literature as applied to temperature observations, such as the separation of the thermal SZ-effect from dominant primordial fluctuations [59].

5.4. CMB-induced Cluster Polarization and Dark Energy. – Secondary CMB polarization in the direction of distant galaxy cluster may provide an opportunity of study the evolution of growth in the late, dark energy dominated universe [49], [50], [60]. This will constrain the time-evolution of the dark energy equation of state and therefore might contribute to a better understanding of the properties and the nature of dark energy.

The basic idea is to use galaxy clusters as tracers of the local temperature quadrupole and statistically detect its rms value. Imagine a future experiment measuring the polarization towards resolved clusters. For each cluster we also measure its redshift and the optical depth through the thermal SZ effect. We do this for a large sample of clusters, bin the resulting data into redshift intervals and average over all sky. If the bin size can

be chosen small enough this will allow us to reconstruct the rms temperature quadrupole as a function of redshift. Multi-frequency observations will allow us to separate the primordial quadrupole from the contaminant kinematic contribution with only a factor of ~ 2 enhancement in the instrumental noise [49].

For the best-fit Λ CDM model with 70% dark energy, the quadrupole leads to a maximum primordial polarization of $P_{\text{Prim}} \sim 4.9\tau \mu\text{K}$. Since the kinematic polarization scales as $P_{\text{Kin}} = 0.27g(x)(\beta_t/0.001)^2\tau \mu\text{K}$, we expect the CMB-induced signal to be dominant (as illustrated in Fig. 7). Factors that could make the primordial and the kinematic polarization more comparable are the frequency boost of the kinematic effect, a more optimistic estimate of $\langle\beta_t\rangle$ and a low value of the CMB-quadrupole. However, even if the signals were of comparable magnitude the random orientations and characteristic frequency dependence of the kinematic polarization would allow a reliable extraction of the primordial CMB-quadrupole.

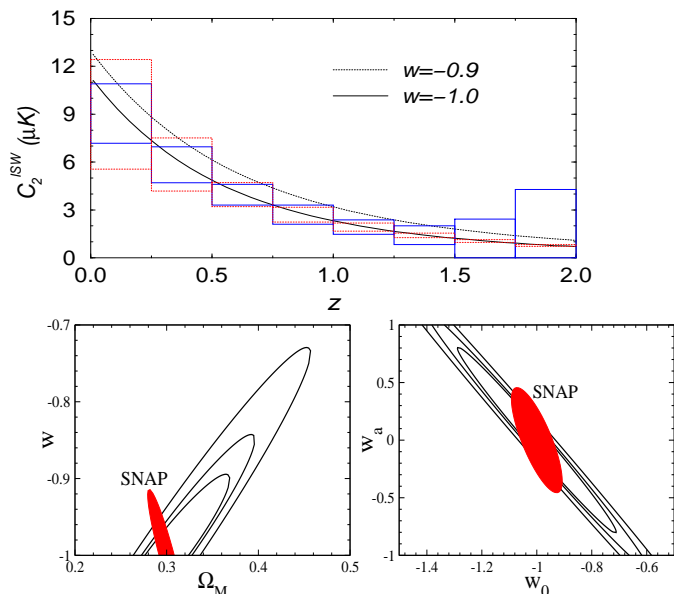


Fig. 9. – *Top panel:* Projected ISW quadrupole as a function of redshift. The solid error bars assume a reconstruction with clusters down to $10^{14} M_\odot$ in an area of 10^4 deg^2 with an instrumental noise of $0.1 \mu\text{K}$. The dotted lines show the cosmic-variance for an all-sky reconstruction computed from the number of independent volumes sampled by clusters at each redshift bin [54]. *Bottom left:* Parameter errors from the projected ISW quadrupole measurements, assuming $w = \text{const}$. The small ellipse is for the case shown in top panel (with cosmic variance added in quadrature), while the two larger ellipses assume a factor of 3 and 10 increase in the instrumental noise contribution, respectively. For comparison, we also show the constraints expected from SNAP. When the most optimistic polarization information is added, SNAP’s constraints on w improve by a factor of 3. *Bottom right:* Same as bottom left, but for w_0 and w_a of the parameterization $w(z) = w_0 + w_a z/(1+z)$ and assuming an additional prior $\sigma(\Omega_M) = 0.01$.

In [49], we assessed the potential detectability of the ISW signature with cluster polarization, while in [60], the measurement of cosmological parameters related to the dark energy using cluster polarization data from, say, the planned CMBpol mission, was discussed. The measurement of dark energy properties is aided by the fact that one probes

the redshift evolution of the ISW contribution through the growth rate of the gravitational potential. The latter provides the most sensitive probe of dark energy when compared to all other cosmological probes considered so far [60]. This comes from the fact that the growth rate of the gravitational potential is directly proportional to the dark energy equation of state, while quantities such as the distance or the growth factor involve, at least, one integral of this quantity.

Establishing the ISW effect and reconstructing its redshift evolution poses a significant experimental challenge. The advent of polarization sensitive bolometers, however, suggests that a reliable reconstruction of the ISW signature is within reach over the next decade. Given the strong dependence of the ISW effect on the background cosmology, cluster polarization can eventually be used as a powerful probe of the dark energy. A detailed analysis of the potential of this method for extracting information on the dark energy equation of state, $w(z)$, is presented in [60] and illustrated in Figure 9.

5.5. Power Spectra of SZ Polarization. – In addition to statistical studies to reconstruct the primordial quadrupole from CMB polarization measurement in the direction of resolved galaxy clusters, in the limit that clusters are unresolved, power spectrum measurements would provide an approach to study the polarization signal. In general, a polarization map will consist of a measurement of the Stokes parameters $Q(\hat{\mathbf{n}})$ and $U(\hat{\mathbf{n}})$ as functions of position $\hat{\mathbf{n}}$ on some patch of the sky. We can construct Fourier components $Q(\mathbf{l})$ and $U(\mathbf{l})$ by

$$(68) \quad X(\mathbf{l}) = \int d^2\hat{\mathbf{n}} e^{i\mathbf{l}\cdot\hat{\mathbf{n}}} X(\hat{\mathbf{n}}),$$

where $X \equiv Q, U$, and \mathbf{l} is a vector in the plane of a region of the sky sufficiently small to be considered flat. Since the Stokes parameters Q and U depend on the choice of axes, we consider the rotationally invariant combinations,

$$(69) \quad \begin{aligned} E(\mathbf{l}) &= \cos(2\phi_1)Q(\mathbf{l}) + \sin(2\phi_1)U(\mathbf{l}) \\ B(\mathbf{l}) &= \cos(2\phi_1)U(\mathbf{l}) - \sin(2\phi_1)Q(\mathbf{l}), \end{aligned}$$

where ϕ_1 is the angle between \mathbf{l} and the chosen x-axis in the plane of the sky. We define the angular power spectra C_l^{EE} and C_l^{BB} from

$$(70) \quad \langle Y(\mathbf{l})Y(\mathbf{l}') \rangle = (2\pi)^2 \delta_D(\mathbf{l} - \mathbf{l}') C_l^{YY},$$

where $Y \equiv E, B$, and the angle brackets denote an average over all realizations of the density field.

If the radiation quadrupole moment is smooth over the region of sky we are considering, then

$$(71) \quad \begin{aligned} \langle E(\mathbf{l})E(\mathbf{l}') \rangle &= \langle B(\mathbf{l})B(\mathbf{l}') \rangle \\ &= \frac{1}{2} (\langle Q(\mathbf{l})Q(\mathbf{l}') \rangle + \langle U(\mathbf{l})U(\mathbf{l}') \rangle), \end{aligned}$$

while

$$(72) \quad \langle E(\mathbf{l})B(\mathbf{l}') \rangle = \frac{1}{2} (\langle Q(\mathbf{l})U(\mathbf{l}') \rangle - \langle Q(\mathbf{l}')U(\mathbf{l}) \rangle) = 0,$$

where the latter equality is consistent with parity conservation. These results can be derived by noting that if the quadrupole moment is constant, then the orientation of the polarization is constant. If so, we may choose our axes on the sky so that $U = 0$. Then, $E(\mathbf{l}) \propto \cos(2\phi_1)$, and $B(\mathbf{l}) \propto \sin(2\phi_1)$, but when averaged over the orientation angle ϕ_1 , we recover Eq. (71).

We now proceed to calculate the power spectra induced by reionization. The polarization in direction $\hat{\mathbf{n}}$ due to scattering from free electrons is an integral along the line of sight [61],

$$(73) \quad Q(\hat{n}) - iU(\hat{n}) = \sqrt{\frac{3}{40\pi}} \int d\eta \frac{d\tau(\eta\hat{\mathbf{n}}, \eta)}{d\eta} a_{22}(\eta),$$

where η is the comoving distance, $(d\tau/d\eta)(\eta\hat{\mathbf{n}}, \eta) = \sigma_T n_e(\eta\hat{\mathbf{n}}, \eta)a(\eta)$, $a(\eta)$ is the scale factor at a comoving distance η , $n_e(\eta\hat{\mathbf{n}}, \eta)$ is the free-electron density at direction $\hat{\mathbf{n}}$ at distance η , and σ_T is the Thomson cross section.

In Eq. (73), $a_{22}(\eta)$ is the radiation quadrupole moment at distance η . More precisely, $a_{22}(\eta)$ is the coefficient of the spherical harmonic $Y_{22}(\theta, \phi)$ in a spherical-harmonic expansion of the radiation intensity in a coordinate system in which the line of sight is the $\hat{\mathbf{z}}$ direction. Note that we take $a_{22}(\eta)$ to be a function of distance only, and not direction, consistent with our assumption that the quadrupole is coherent over a large patch of the sky. Since we use Limber's approximation below, in which angular correlations are induced only by spatial separations at the same distance, the variation of $a_{22}(\eta)$ with distance can be included consistently.

With the polarization written as a projection along the line of sight, Eq. (73), the angular power spectrum follows in the flat-sky limit from Limber's equation [21],

$$(74) \quad \begin{aligned} C_l^{EE} &= C_l^{BB} \\ &= \frac{3}{80\pi} \int_0^{z_{\text{rei}}} dz \frac{d^2V}{d\Omega dz} |a_{22}(z)|^2 P_{\tau\tau}^{(t)} \left(\frac{l}{d_A}, z \right), \end{aligned}$$

where $P_{\tau\tau}^{(t)}$ is the power spectrum of $d\tau/d\eta$, proportional to the power spectrum of the electron density n_e , and the integral is taken up to the redshift z_{rei} of reionization using the comoving differential volume given by $d^2V/d\Omega dz$.

In Fig. 8, we summarize results related to the polarization power spectra from galaxy clusters. In the case of the primordial quadrupole, we replace $|a_{22}(z)|^2$ in Eq. (74) by its expectation value, $C_2^{\Theta\Theta}(z)$, the variance of the temperature quadrupole at redshift z (shown in Fig. 6). In the case of the kinematic quadrupole, we replace $|a_{22}(z)|^2$ by the expectation value of equation (67),

$$(75) \quad \langle |a_{22}|^2 \rangle = \frac{4\pi}{30} g^2(x) \langle v_t^4 \rangle = \frac{16\pi}{135} g^2(x) v_{\text{rms}}^4,$$

where we have used $\langle v_t^4 \rangle = \langle (v_x^2 + v_y^2)^2 \rangle = (8/9)v_{\text{rms}}^4$, since $\langle v_x^2 \rangle = \langle v_y^2 \rangle = v_{\text{rms}}^2/3$, $\langle v_x^4 \rangle = \langle v_y^4 \rangle = 3\langle v_x^2 \rangle^2 = v_{\text{rms}}^4/3$, and $\langle v_x^2 v_y^2 \rangle = \langle v_x^2 \rangle \langle v_y^2 \rangle = v_{\text{rms}}^4/9$. We calculate the linear-theory rms peculiar velocity by integrating over the power spectrum, as in the case of the SZ kinetic temperature anisotropy calculation. According the halo-clustering model [16], peculiar-velocity fields are correlated over large distances and the non-linear corrections to v_{rms}^2 are small. The resulting linear-theory rms kinematic quadrupole is also shown

in Fig. 6 assuming $g(x) = 1$ as relevant for Rayleigh-Jeans (RJ) part of the frequency spectrum when $x \rightarrow 0$, and for $\nu = 150$ GHz and $\nu = 220$ GHz.

In Fig. 8, note that the secondary polarization discussed here contributes equally to E- and B-modes (cf. equation (74)). While the 1-halo term dominates at arcminute angular scales and below, correlations between halos are important and determine the total effect due to secondary polarization at angular scales corresponding to a few degrees. The dependence of our results on the inclusion of the 2-halo term is consistent with the result obtained for the temperature power spectra from the kinetic SZ effect [14], while it is inconsistent with the thermal SZ effect, where contributions are dominated by the 1-halo term over the whole range of angular scales. The latter behavior is explained by the fact that the thermal SZ effect is highly dependent on the most massive halos, while the kinetic SZ effect, and the secondary polarization signals calculated here, are independent of the gas temperature and thus can depend on halos with a wider mass range.

As shown in Fig. 8, the secondary E-mode polarization is several orders of magnitude below the E polarization from the surface of last scattering. The secondary polarization is therefore unlikely to be a source of confusion when interpreting polarization contributions to E-modes. The amplitude of the primary effect in B-modes, due to gravitational waves, is highly uncertain and depends on the energy scale of inflation [62]. For illustration, we show in Fig. 8 the inflationary gravitational wave (IGW) signal assuming an energy scale for inflation of $E_{\text{infl}} = 10^{16}$ GeV, where the amplitude of the power spectrum scales as E_{infl}^4 . At large angular scales the secondary polarization is several orders of magnitude below the peak of this hypothetical IGW polarization signal. If the energy scale of inflation is lowered considerably, say to $E_{\text{infl}} < 10^{15}$ GeV, then we might guess that the secondary polarization could ultimately constitute a background.

As also shown in Fig. 8, however, there is a contribution to the B-mode power spectrum that arises from conversion of the primary E-modes to B-modes by gravitational lensing [63], and this is considerably larger than the secondary polarization from galaxy clusters. Moreover, we also show (the dot-dash curve) the contribution to the irreducible B-mode power spectrum that remains even after the lensing has been optimally subtracted with higher-order correlations [64, 65, 66, 67]. This residual lensing power spectrum is considerably larger than the polarization from reionization. Thus, the secondary SZ polarization effects are unlikely to be a factor for either gravitational-lensing or gravitational-wave studies with B-modes.

* * *

AC thanks the organizers of the summer school, F. Melchiorri and Y. Rephaeli, for an enjoyable and productive conference and for the invitation to present the research discussed in this review. We would like to thank Marc Kamionkowski and Dragan Huterer for important collaboration upon which parts of this review are based.

REFERENCES

- [1] R. A. Sunyaev and Ya. B. Zel'dovich, *MNRAS* **190**, 413 (1980).
- [2] W. L. Freedman *et al.*, *Astrophys. J.* **553**, 47 (2001).
- [3] D. N. Spergel *et al.*, preprint [arXiv:astro-ph/0302209].
- [4] J. E. Carlstrom, M. Joy and L. Grego, *Astrophys. J.*, **456**, L75 (1996).
- [5] M. Jones, R. Saunders, P. Alexander *et al.*, *Nature*, **365**, 320 (1993).

- [6] N. Kaiser, *Astrophys. J.*, **282**, 374 (1984).
- [7] A. R. Cooray and W. Hu, [arXiv:astro-ph/9910397].
- [8] J. P. Ostriker and E. T. Vishniac, *ApJ*, 306, L51 (1986); E. T. Vishniac, *Astrophys. J.*, **322**, 597 (1987).
- [9] N. Aghanim, F. X. Desert, J. L. Puget and R. Gispert, [arXiv:astro-ph/9604083].
- [10] A. Gruzinov and W. Hu, [arXiv:astro-ph/9803188].
- [11] M. G. Santos, A. Cooray, Z. Haiman, L. Knox and C. P. Ma, *Astrophys. J.* **598**, 756 (2003) [arXiv:astro-ph/0305471].
- [12] S. Cole and N. Kaiser, *Mon. Not. Roy. Astron. Soc.* **233**, 637 (1988); E. Komatsu and T. Kitayama, *Astrophys. J.* **526**, L1 (1999).
- [13] A. Cooray, *Phys. Rev. D* **62**, 103506 (2000).
- [14] A. Cooray, *Phys. Rev. D* **64**, 043516 (2001).
- [15] E. Komatsu and U. Seljak, *Mon. Not. Roy. Astron. Soc.* **336** 1256 (2002).
- [16] A. Cooray and R. Sheth, *Phys. Rept.* **372**, 1 (2002) [arXiv:astro-ph/0206508].
- [17] E. Komatsu and U. Seljak, *Mon. Not. Roy. Astron. Soc.* **327** 1353 (2002).
- [18] M. White, L. Hernquist, and V. Springel, preprint [arXiv:astro-ph/0205437].
- [19] D. Eisenstein and W. Hu, *Astrophys. J.* **511**, 5 (1999).
- [20] H. J. Mo, Y. P. Jing, and S. D. M. White, *Mon. Not. Roy. Astron. Soc.* **284**, 189 (1997).
- [21] D. Limber, *Astrophys. J.* **119**, 655 (1954).
- [22] W. H. Press and P. Schechter, *Astrophys. J.* **187**, 425 (1974);
- [23] R. K. Sheth and G. Tormen, *Mon. Not. Roy. Astron. Soc.* **308**, 119 (1999).
- [24] J. P. Henry, *Astrophys. J.* **534**, 565 (2000).
- [25] J. Navarro, C. S. Frenk, and S. D. M. White, *Astrophys. J.* **462**, 563 (1996); B. Moore, T. Quinn, F. Governato, J. Stadel, and G. Lake, *Mon. Not. Roy. Astron. Soc.* **310**, 1147 (1999).
- [26] J. S. Bullock, T. S. Kolatt, Y. Sigad, R. S. Somerville, A. V. Kravtsov, A. A. Klypin, J. R. Primack, A. Dekel, *Mon. Not. Roy. Astron. Soc.* **321**, 559 (2001); R. H. Wechsler, J. S. Bullock, J. R. Primack, A. V. Kravtsov, A. Dekel, *Astrophys. J.* **568**, 52 (2002); Y. P. Jing and Y. Suto, *Astrophys. J. Lett.* **529**, 69 (2000).
- [27] L. Verde, M. Kamionkowski, J. J. Mohr, and A. J. Benson, *Mon. Not. Roy. Astron. Soc.* **321**, L7 (2001).
- [28] C. S. Frenk et al., *Astrophys. J.* **525**, 554 (1999).
- [29] B. S. Mason et al., preprint [arXiv:astro-ph/0205384].
- [30] K. S. Dawson et al., preprint [arXiv:astro-ph/0206012].
- [31] J. R. Bond et al., preprint [arXiv:astro-ph/0205386].
- [32] A. Cooray and W. Hu, *Astrophys. J.* **554**, 56 (2001) [arXiv:astro-ph/0012087].
- [33] U. Seljak, J. Burwell, and U. -L. Pen, *Phys. Rev. D* **63**, 063001 (2001).
- [34] G. P. Holder, *Astrophys. J.* **578**, L1 (2002) [arXiv:astro-ph/0207633].
- [35] S. P. Oh, A. Cooray and M. Kamionkowski, *Mon. Not. Roy. Astron. Soc.* **342**, L20 (2003) [arXiv:astro-ph/0303007].
- [36] *Phys. Rev. D* **66**, 083001 (2002) [arXiv:astro-ph/0204250].
- [37] D. N. Spergel and D. M. Goldberg, *Phys. Rev. D* **59**, 103001 (1999); D. M. Goldberg and D. N. Spergel, *Phys. Rev. D*, **59**, 103002 (1999); M. Zaldarriaga and U. Seljak, *Phys. Rev. D*, **59**, 123507 (1999); H. V. Peiris and D. N. Spergel, *Astrophys. J.*, **540**, 605 (2000).
- [38] A. Cooray, *Phys. Rev. D* **64**, 043516 (2001) [arXiv:astro-ph/0105415].
- [39] Dodelson, S. Jubas, *J. M.* 1995, *ApJ*, **439**, 503.
- [40] Jaffe, A. H., Kamionkowski, M. 1998, *Phys. Rev. D.*, **58**, 043001.
- [41] Hu, W., Scott, D., Sugiyama, N., White, M. 1995, *Phys. Rev. D.*, **52**, 5498.
- [42] V. Springel, M. J. White and L. Hernquist, [arXiv:astro-ph/0008133].
- [43] A. C. d. Silva, D. Barbosa, A. R. Liddle and P. A. Thomas, *Mon. Not. Roy. Astron. Soc.* **326**, 155 (2001) [arXiv:astro-ph/0011187].
- [44] A. Cooray and X. I. Chen, *Astrophys. J.* **573**, 43 (2002) [arXiv:astro-ph/0107544].
- [45] D. Nagai, A. V. Kravtsov and A. Kosowsky, *Astrophys. J.* **587**, 524 (2003) [arXiv:astro-ph/0208308].
- [46] A. Kogut *et al.*, preprint [arXiv:astro-ph/0302213].

- [47] W. Hu, *Astrophys. J.* **529**, 12 (2000).
- [48] D. Baumann, A. Cooray and M. Kamionkowski, *New Astron.* **8**, 565 (2003) [arXiv:astro-ph/0208511].
- [49] A. Cooray and D. Baumann, *Phys. Rev. D* **67**, 063505 (2003) [arXiv:astro-ph/0211095].
- [50] D. Baumann and A. Cooray, *New Astron. Rev.* **47**, 839 (2003) [arXiv:astro-ph/0304416].
- [51] S. Y. Sazonov and R. A. Sunyaev, *MNRAS* **310**, 765 (1999).
- [52] A. Challinor, M. Ford, and A. Lasenby, *MNRAS* **312**, 159 (2000).
- [53] E. Audit and J. F. L. Simmons, *MNRAS* **305**, L27 (1999).
- [54] M. Kamionkowski and A. Loeb, *Phys. Rev. D* **56**, 4511 (1997); N. Seto and M. Sasaki, *Phys. Rev. D* **62**, 123004 (2000) [arXiv:astro-ph/0009222];
- [55] J. Portsmouth, *Phys. Rev. D* **70**, 063504 (2004) [arXiv:astro-ph/0402173].
- [56] R. K. Sachs and A. M. Wolfe, *Astrophys. J.* **147**, 73 (1967).
- [57] C. L. Bennett et al., *Astrophys. J.* **436**, 423 (1994).
- [58] S. Dodelson, *Astrophys. J.* **482**, 577 (1997).
- [59] A. Cooray, W. Hu, and M. Tegmark, *Astrophys. J.* **540**, 1 (2000).
- [60] A. Cooray, D. Huterer, and D. Baumann, preprint [arXiv:astro-ph/0304268].
- [61] A. Kosowsky, *Ann. Phys.* **246**, 49 (1996).
- [62] See, for example, M. Kamionkowski and A. Kosowsky, *Annu. Rev. Nucl. Part. Sci.* **49**, 77 (1999), and references therein.
- [63] M. Zaldarriaga and U. Seljak, *Phys. Rev. D* **58**, 023003 (1998).
- [64] M. Kesden, A. Cooray and M. Kamionkowski, *Phys. Rev. Lett.* **89**, 011304 (2002) [arXiv:astro-ph/0202434].
- [65] L. Knox and Y. S. Song, *Phys. Rev. Lett.* **89**, 011303 (2002).
- [66] A. Cooray and M. Kesden, *New Astron.* **8**, 231 (2003) [arXiv:astro-ph/0204068]; M. Kesden, A. Cooray and M. Kamionkowski, *Phys. Rev. D* **67**, 123507 (2003) [arXiv:astro-ph/0302536].
- [67] U. Seljak and M. Zaldarriaga, *Phys. Rev. Lett.* **82**, 2636 (1999); W. Hu, *Phys. Rev. D* **64**, 083005 (2001); W. Hu and T. Okamoto, [arXiv:astro-ph/0111606]; C. M. Hirata and U. Seljak, *Phys. Rev. D* **67**, 043001 (2003) [arXiv:astro-ph/0209489].